Phase diagram of carbon-nickel-tungsten: A superatom model

Sanxi Yao, Qin Gao, and Michael Widom

Department of Physics, Carnegie Mellon University, Pittsburgh, Pennsylvania 15213, USA

Christopher Marvel and Martin Harmer

Department of Materials Science and Engineering, Lehigh University, Bethlehem, Pennsylvania 18015, USA

Carbon solubility in face-centered-cubic Ni-W alloys and the phase diagrams of Ni-W and C-Ni-W are investigated by means of first principles calculations and semigrand canonical Monte Carlo simulations. With density functional theory total energies as fitting data, we build a superatom model for efficient simulation. Multihistogram analysis is utilized to predict free energies for different compositions and temperatures. By comparing free energies of competing phases, we are able to predict carbon solubility and phase diagrams of C-Ni-W at different temperatures. A simple ideal mixing approximation gives qualitatively similar predictions.

I. INTRODUCTION

Nickel-tungsten (Ni-W) alloys have gained interest recently due to their unusual mechanical, electrical, and corrosion properties, including high hardness, melting temperature, and corrosion resistance [1–3]. W atoms dissolve in the fcc matrix of Ni [4], even though the stable pure W structure has a bcc lattice [5]. Owing to their limited grain growth at elevated temperature, Ni-W alloys are considered to be thermally stable [6]. Three Ni-W phases are experimentally reported [7]: Ni_4W, NiW, and NiW_2. However, the NiW and NiW_2 phases are actually carbon nickel tungsten (C-Ni-W) phases CNi_6W_6 and CNi_2W_4 [8]. The Mo-Ni phase diagram displays a similar composition range and Ni_4Mo phase [9]. A recent theoretical study [10] reports a tendency for tungsten atoms to order along chains in the $\langle 100 \rangle$ direction to form a Pt_8Ti phase, and also predicts possible stable structures with W compositions larger than 20 at. %. The Pt_8Ti-type structures is also suggested by x-ray scattering off the Fermi surface [11]. Considering common impurities, carbon has strong interaction with Ni-W [12], leading to formation of C-Ni-W phases at low carbon concentration.

To study carbon solubility in fcc Ni-W, we calculate the energies of Ni-W structures and fit an energy model. We then perform semigrand canonical Monte Carlo simulation to study the phase stability of Ni-W as well as C-Ni-W with carbon at octahedral interstitial sites. We also make predictions about the tungsten solubility range as a function of temperature for the Ni-W binary. By studying the effect of impurities like carbon, we propose an explanation to why the Ni_8W phase, which is stable from calculation, is not observed in experiment, and then show our predicted phase diagrams of the C-Ni-W ternary at several temperatures, with both Monte Carlo simulation and ideal mixing approximation methods.

II. METHODS

A. First principle calculation and convex hull of Ni-W

We use the density functional theory-based Vienna *ab initio* simulation package (VASP) [13–16] to calculate total energies within the projector augmented wave (PAW) [17,18] method, utilizing the PBE generalized gradient approximation [19,20] as the exchange-correlation functional. We construct a variety of supercells, about 440 Ni-W binary structures in all, which we relax with increasing k-point meshes until convergence is reached at the level of 0.1 meV/atom, holding the plane-wave energy cutoff fixed at 270 eV. For phonon calculation, we increase the cutoff energy to 330 eV and use a smaller energy tolerance to ensure better convergence. A few special C-Ni-W structures are made and calculated to evaluate the nearest neighbor carbon-carbon and carbon-tungsten repulsion. For the C-Ni-W ternary the cutoff energy is 400 eV.

Figures 1 and 2 show the enthalpy of formation ΔH vs the W composition, where ΔH is the energy of the structure with respect to pure elemental ground state structures, fcc Ni.cF4 and bcc W.cI2. In Fig. 1 we can see that fcc W, NiW, and NiW_2 have high energy; thus they are unstable. Any structure with ΔH above the convex hull will decompose into the end-point structures on the convex hull. We define $\Delta\Delta H$ as ΔH of the structure relative to the convex hull at the same composition. For the stable binary structures, Ni_8W.tI18 and Ni_4W.tI10 have 11 at. % and 20 at. % W, respectively. Two other structures suggested by reports in the literature [10] are also on the convex hull, with W content slightly higher than 20 at. % as shown in Fig. 2, consistent with their conclusion that Ni-W forms stable and metastable compounds over a wide composition range. These four stable structures all share a feature of columns formed by W atoms along $\langle 100 \rangle$ directions [10]. Variants made by displacing complete W columns also have small positive $\Delta\Delta H$.

B. Superatom model

We build a model to map fcc-based Ni-W structures to relaxed total energies. Our superatom model [21] includes local environments of Ni and W atoms, as well as longer-range pair interactions. To represent pairwise interactions of Ni-W, only W-W pairs need to be considered, because for any given length bond the numbers of Ni-Ni and Ni-W pairs are functions of the number of W-W pairs, along with the system size and the W concentration. We include pair interactions up to the five shortest bond lengths. Secondly, for each atom, we consider the environment around that atom up to the next nearest neighbor, and call it a superatom (Fig. 3). Ni-centered
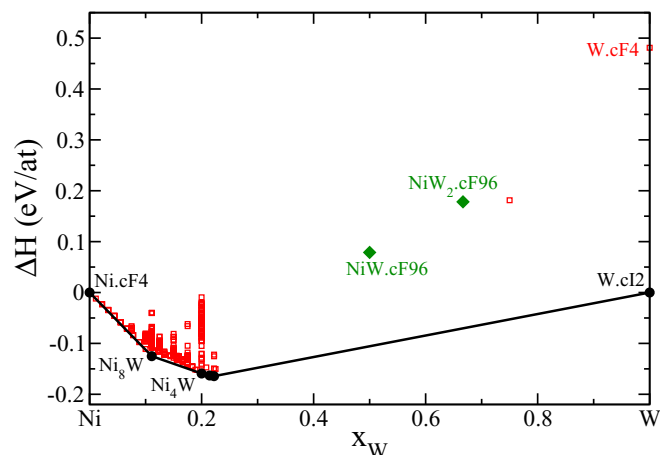
FIG. 1. Enthalpies of formation in the Ni-W binary alloy. Black lines and circles show the convex hull. Red squares are fcc-based structures lying above the convex hull. Green diamonds are NiW and $NiW_2.cF96$.

superatoms have variable occupation of 12 nearest neighbor sites resulting in 10 symmetry-independent cases. W-W near neighbor bonds are strongly unfavorable, so we define W-centered superatom to have only Ni as nearest neighbors. The pair interactions capture the energies of unfavorable cases with nearest-neighbor W-W bonds that occur only infrequently. The six next-nearest neighbors have variable occupancy, resulting in 10 symmetry-independent types. Figure 11 illustrates the twenty types of superatoms considered in our model. Our superatom model includes complex many-body interactions that cannot be conveniently represented using a complete cluster expansion.

As a result, the superatom model contains 26 features: the number of W atoms, the numbers of five shortest W-W pairs, and the numbers from 20 types of superatoms. The energy model is then expressed in the linear form:

$$E(\vec{n}) = \sum_{i=0}^{26} \beta_i n_i = \vec{n} \cdot \vec{\beta}. \qquad (1)$$
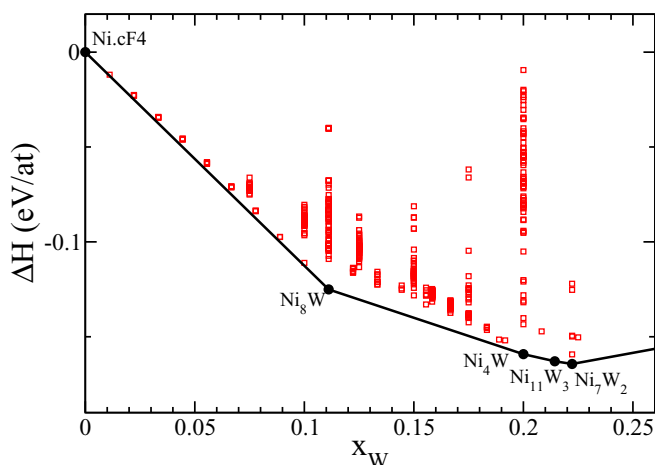

FIG. 2. Details of enthalpies up to 25% W. Plotting symbols as in Fig. 1.

Here E is the energy per atom, while $\vec{n}$ is the count of certain pairs or superatoms, divided by the total number of atoms. n_0 is always 1, corresponding to an overall energy shift, n_1 is W composition, n_2 to n_6 are the counts of W-W pairs scaled to per atom, and n_7 to n_{26} are the counts of superatoms scaled to per atom. Components of $\vec{\beta}$ are the corresponding fitting parameters.

Our fitting procedure minimizes the weighted-mean-square deviation of model energy from calculated density functional theory (DFT) energy [22], where the weight is chosen as an exponential of $\Delta\Delta H$

$$\beta^* = \arg\min_{\vec{\beta}} \sum_{\alpha} (e^{-\frac{\Delta\Delta H_\alpha}{k_B T}} (\Delta H_\alpha - \vec{n}_\alpha \cdot \vec{\beta}))^2. \qquad (2)$$

Here ΔH_α is the enthalpy of formation for structure α, taking pure element structures as the reference points, and $\Delta\Delta H_\alpha$ is the energy above the convex hull. Here $T = 200$ K is a fictitious temperature used to diminish the weight of high energy structures. Our fit yields a fivefold cross validation error around 2 meV/atom, corresponding to an uncertainty in temperature of about 23 K. Fivefold cross validation means we leave one-fifth of structures out for testing and repeat the process five times. The comparison between DFT and model is shown in Fig. 4.

C. Monte Carlo simulation and multihistogram method

We perform conventional Metropolis Monte Carlo simulations with 90 atoms in a $3\sqrt{5} \times 3\sqrt{5} \times 1$ supercell, with 180 atoms (double along z axis), 270 atoms (triple along z axis), and 360 atoms (quadruple along z axis). This supercell was chosen to be commensurate with both $Ni_8W.tI18$ and $Ni_4W.tI10$ structures. The basic move is to randomly pick a site and change the species (Ni to W, or W to Ni). Moves are accepted or rejected according to the Boltzmann factor for the energy change ΔE and chemical potential change $\mu\Delta N_W$. Here $\Delta N_W = -1$ when we pick a W atom and change it to Ni and $\Delta N_W = +1$ vice versa. The Boltzmann factor is $\exp(-(\Delta E - \Delta N_W \mu)/k_B T)$ where $\mu \equiv \mu_W - \mu_{Ni}$.

For the Ni-W binary, where Ni and W sit at fcc lattice sites, we construct about 440 Ni-W structures with W composition ranging from 0 to 23 at. %, and take the energies to fit an energy model for simulation. In the C-Ni-W ternary, C atoms sit at octahedral sites of the fcc lattice, surrounded by six nearest metal (Ni/W) sites. Carbon-carbon and carbon-tungsten repulsion are added to the binary energy model. We then perform semigrand canonical Monte Carlo simulation to study the phase stability of C-Ni-W phase at different temperatures, holding fixed the total number of metal atoms and, in the ternary, the total number of carbon atoms.

Multidimensional replica exchange can help avoid getting stuck in competing states. For a selection of simulation trajectories, suppose the ith one is at temperature T_i and chemical potential μ_i, with total energy E_i and tungsten number N_i, and the jth one has similar corresponding features with subscript j. The probability of occurrence of these two trajectories is proportional to the corresponding Boltzmann
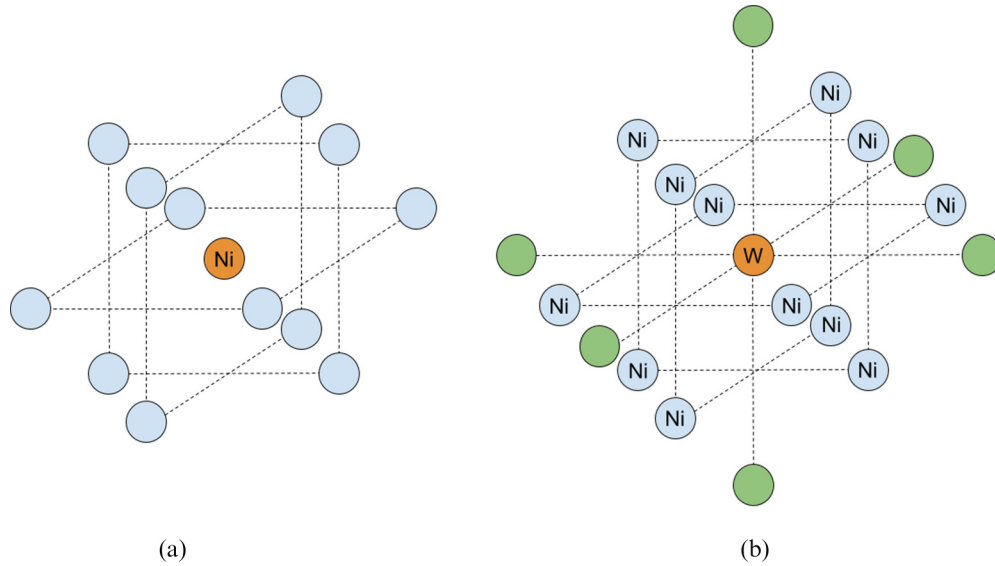
FIG. 3. (a) Superatom with central Ni atom and variable occupation of neighbors (blue). (b) Superatom with central W atom, Ni first neighbors, and variable occupation of second neighbors (green).

factor

$$P_1 = P_i(T_i, \mu_i) P_j(T_j, \mu_j) \propto e^{-(E_i - N_i \mu_i)/k_B T_i} e^{-(E_j - N_j \mu_j)/k_B T_j}.$$

(3)

If we swap these two trajectories, so that trajectory i takes T_j and μ_j, and trajectory j takes T_i and μ_i, then the probability is

$$P_2 = P_i(T_j, \mu_j) P_j(T_i, \mu_i) \propto e^{-(E_i - N_i \mu_j)/k_B T_j} e^{-(E_j - N_j \mu_i)/k_B T_i}.$$

(4)

So the acceptance probability to interchange the trajectories is

$$P = P_2/P_1 = e^{\Delta\beta\Delta E - \Delta N \Delta(\beta\mu)},$$

(5)

where we define $\Delta\beta = 1/(k_B T_i) - 1/(k_B T_j)$, $\Delta E = E_i - E_j$, $\Delta N = N_i - N_j$, and $\Delta(\beta\mu) = \mu_i/(k_B T_i) - \mu_j/(k_B T_j)$.

We analyze the Monte Carlo results using a multidimensional variant of the multihistogram method [23,24], similar to the one-dimensional analysis in our previous work on the boron carbide system [25]. At temperature T and chemical potential μ, the histogram of configurations with energy E and tungsten composition x, $H_{T,\mu}(E, x)$, can be converted into a density of states $W(E, x) = H_{T,\mu}(E, x)\exp((E - \mu x N)/k_B T)$, where N is the total number of atoms. Here we fix T, and combine the histograms from different chemical potentials μ_i to evaluate the density of states. Then we can evaluate the partition function

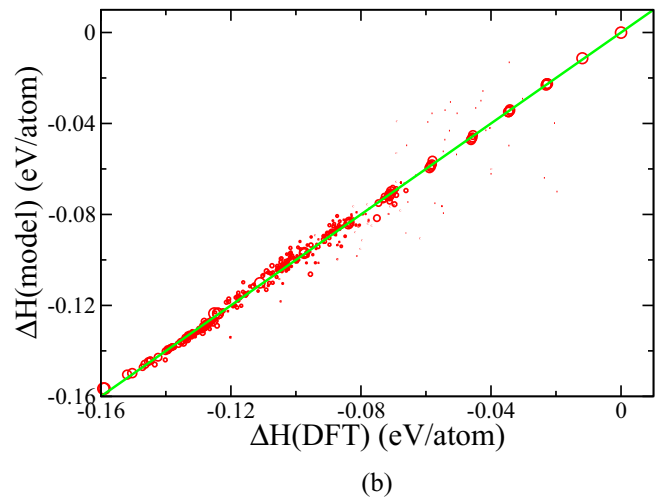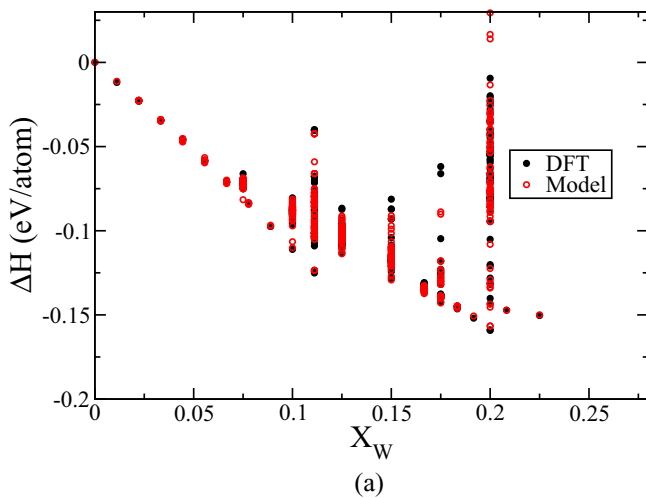$$Z(T, \mu) = \sum_{E,x} W(E, x) e^{-(E - \mu x N)/k_B T},$$

(6)

FIG. 4. Comparison between DFT and superatom model. (a) Enthalpy of formation ΔH as a function of W composition calculated via DFT (black circles) or predicted with the model (red circles). (b) Comparison of DFT and superatom model; the size of circles indicates the weights in the fitting.
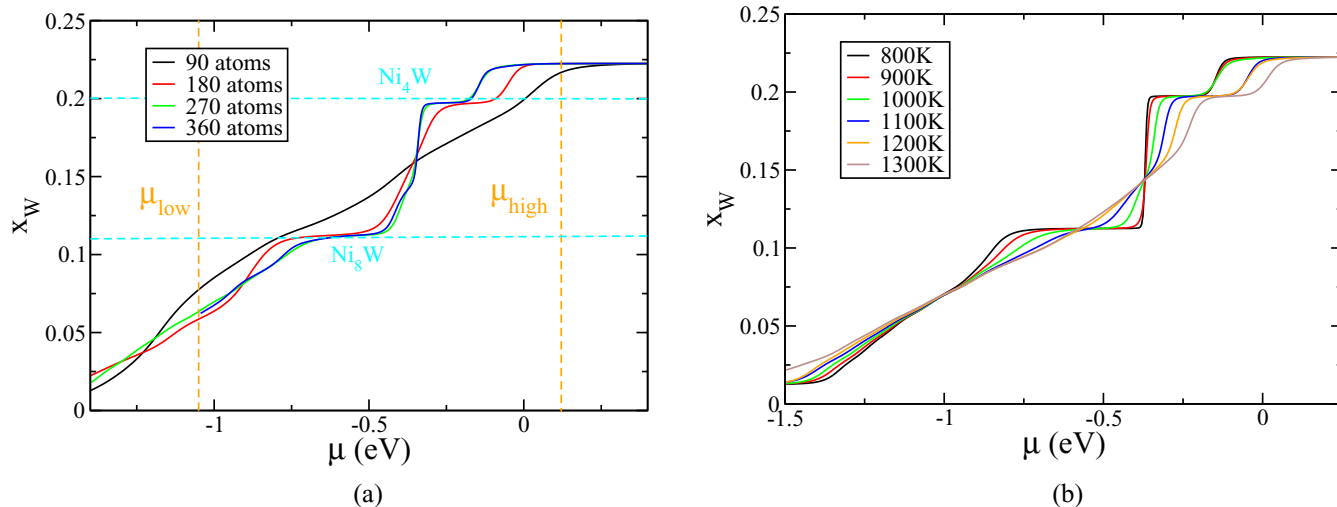
(a)

(b)

FIG. 5. (a) Tungsten composition x_W as a function of μ for different system sizes at $T = 1000$ K; vertical orange dash line shows the real chemical potential limit at this temperature. (b) For system with 270 atoms, x_W as a function of μ at different temperatures.

which is accurate over a range of chemical potentials covering all μ_i's, as long as the histograms of nearby μ's overlap. Composition x_W can be obtained by differentiating the free energy $F = -k_B T \ln Z$ with respect to μ.

III. RESULTS AND DISCUSSION

A. Ni-W binary simulation

We perform Ni-W binary simulations for systems with 90, 180, 270, and 360 atoms, at different temperatures and chemical potentials, supplemented with two-dimensional replica exchange in T and μ to reach better equilibrium. By comparing the stable structures on the convex hull, Ni.cF4, Ni$_8$W.tI18, Ni$_4$W.tI10, and W.cI2, including temperature dependent corrections from vibrational free energy and electronic free energy, we determine that the chemical potential μ should be in a range of -1.1 eV through $+0.16$ eV at $T = 500$ K and change to -1.0 eV through $+0.11$ eV at $T = 1200$ K. We then choose a selection of μ's that covers that range.

Figure 5 shows the predicted tungsten composition x_W as a function of μ for different system sizes (a) and at different temperatures (b). At $T = 1000$ K, the system with 90 atoms may be a little too small to show distinguishable Ni$_8$W and Ni$_4$W phases, while in larger systems those phases cover a range of μ. The x_W curves for a system with 270 and 360 atoms are overlapping, indicating that the finite size effect diminishes.

Figure 5(b) shows x_W for a system of 270 atoms ($3\sqrt{5} \times 3\sqrt{5} \times 3$ supercell). As temperature increases, the Ni$_8$W phase begins to disorder around 1100 K, while Ni$_4$W remains ordered until 1300 K, but shifts towards high μ. The high μ end, which is between 0.11 eV and 0.16 eV and temperature dependent, always goes beyond 20 at. % of x_W. Our first principles calculation in Fig. 2 displays some stable structures beyond Ni$_4$W, supporting this result.

Figure 6 shows the simulated binary phase diagram for systems with 270 atoms. Each point represents our predicted x_W at one particular temperature and chemical potential. Regions of nearly constant concentration (as determined heuristically

by eye) are shown in color, and rapidly varying concentrations corresponding to coexistence regions are shown in gray.

B. Ni-W simulation with carbon

Experimental studies conducted at Lehigh University have covered many aspects of nanocrystalline Ni-W alloys [26], including grain growth, thermal stability, and the effect of processing. Their study quantified the impurity concentration of carbon, oxygen, and sulfur in electron deposited alloys with hot extraction analysis, and determined that both carbon and oxygen concentrations reach up to 0.5 at. %, while sulfur can be ignored relative to carbon and oxygen. Other light elements like nitrogen can also be present. Treating other impurities similarly as carbon, in affecting the thermal stability of C-Ni-W, we simulate up to 3.5 at. % total impurity concentration.

We add carbon at octahedral interstitial sites in the fcc lattice then conduct semigrand canonical simulations where the number of carbon atoms is fixed, while the numbers of
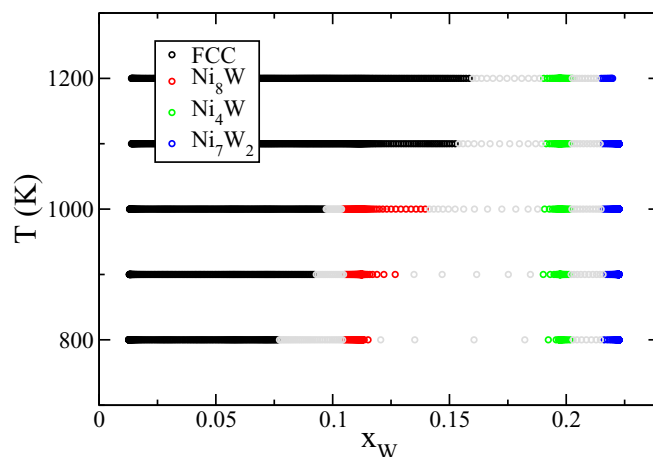

FIG. 6. Ni-W phase diagram in the x_W-T plane for systems containing 270 atoms. Four phases are identified: fcc high Ni solid solution (black), Ni$_8$W (red), Ni$_4$W (green), and Ni$_7$W$_2$ (blue). Gray represents phase coexistence.
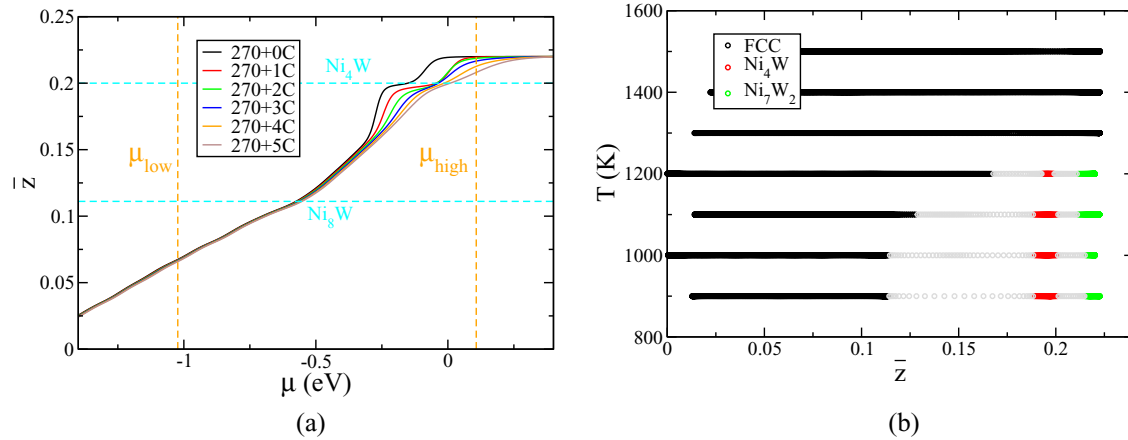
FIG. 7. (a) $\bar{z}$ as a function of μ for the system with 270 Ni/W atoms with different number of carbons at $T = 1200$ K. (b) Ni-W phase diagram in the $\bar{z}$-T plane for the system with 270 Ni/W atoms plus two carbon atoms. Phases are labeled as in Fig. 6.

nickel and tungsten atoms are varied with their total number constant. There are two additional parameters in the energy model involving carbon: the energy of the shortest C-W bond and the energy of the shortest C-C bond. Both are repulsive and estimated from DFT calculation with the values 0.583 eV/bond and 0.302 eV/bond relative to C-Ni bonds, respectively. These bond energies are obtained from structures with 90 metal sites with one or two carbons, by comparing the energy of structures with the near-neighbor bond to the energy of structures of the same composition without that bond.

Figure 7(a) shows the predicted tungsten composition for the system with 270 metal atoms with different numbers of additional carbon atoms. Here we take the tungsten composition as the number of W atoms scaled by the total number of W and Ni atoms, without including the additional carbon atoms. We define this quantity as $\bar{z} = z/(y + z)$ for the ternary phase $C_x Ni_y W_z$. At the high μ end, adding carbon decreases x_W, dropping the high μ limit of the Ni-W phase to 20 at.%. Figure 7(b) displays the predicted phase diagram in the case with 270 Ni/W atoms and two carbon atoms, showing that $Ni_8 W$ merges into the fcc solid solution, leaving a gap between the fcc solid solution and $Ni_4 W$ (i.e., a solubility limit for the Ni-W solid solution of ~11 at.% W, consistent with experiment [7]) at T below 1000 K, and these two phases merge at higher temperature. This means that the $Ni_8 W$ phase disappears in the presence of carbon, which could be a reason why the $Ni_8 W$ phase is not observed in experiments.

C. C-Ni-W ternary phase diagram

Based on the free energies obtained from the simulation results, and by comparing the free energy of C-Ni-W phase with that of competing phases, we can predict the C-Ni-W ternary phase diagram. Besides elemental fcc Ni, bcc W, and hexagonal C, we include two special ternary structures $CNi_2 W_4.cF112$ and $CNi_6 W_6.cF104$, corresponding to the two previously proposed stable binaries NiW_2 and NiW [7], respectively. These two ternaries are predicted to be stable at finite temperature. Thus we propose that the reported NiW and NiW_2 phases are stabilized by C impurities. Both $CNi_2 W_4.cF112$ and $CNi_6 W_6.cF104$ are derived from binary $NiW.cF96$, with carbon atoms sitting at octahedral interstitial

sites, fully surrounded by W atoms (contrary to the fcc solid solution, where C likes to be associated with Ni atoms). There are three types of Wyckoff positions in $NiW.cF96$ structures, with Ni sitting at two types of icosahedral sites, while W is at Frank-Kasper type Z14 sites [27]. W occupy one of the icosahedral sites in the case of NiW_2. Ni-W substitution is less costly in $CNi_2 W_4$ than in $CNi_6 W_6$, leading to a small range of solid solution around $CNi_2 W_4$ at elevated temperature [28]. A different type of structure with stoichiometry $C_7 Ni_6 W_{20}.hP34$ is calculated to be metastable, and can be stabilized by phonon vibrational entropy at finite temperature. For the C-W binary line, our calculation shows the ΔH of CW_2 is high, about 68 meV/atom above the convex hull. Experimentally the CW_2 phase, which has intrinsic disorder, only appears above 1250 °C [29].

Multiple histogram analysis of simulations predict free energies for systems with a fixed of carbon atoms. However, this free energy has an unknown reference as a function of the number of carbons. For a specific number of carbon atoms, we predict the free energy ΔF as a function of $\bar{z} = x_W/(x_W + x_{Ni})$. The free energy along the C-Ni line can be estimated with the linearly interpolated energy and ideal mixing approximation of entropy. Matching the lines of ΔF's with C-Ni line, we can put our predicted free energy on a unified relative scale, and determine the stable structures as those on the convex hull of F. Figure 8 shows an example from the system with 270 Ni/W sites. Part (a) shows free energies from simulations with different numbers of carbon atoms, while (b) shows the stable compositions of the C-Ni-W fcc solid solution as a set of red lines.

The predicted ternary phase diagrams at $T = 1200$ K and $T = 1600$ K are displayed in Fig. 9. At 1200 K, there is a small region of fcc. As temperature increases to 1600 K, the carbon solubility increases and the fcc phase region expands. The solubility expansion can also be seen along the Ni-W binary line by comparing these two phase diagrams.

D. Constrained ideal mixing approximation model

A simple free energy model was also constructed to compare with our simulation and interpret the results. This model also allows us to generalize to temperatures at which
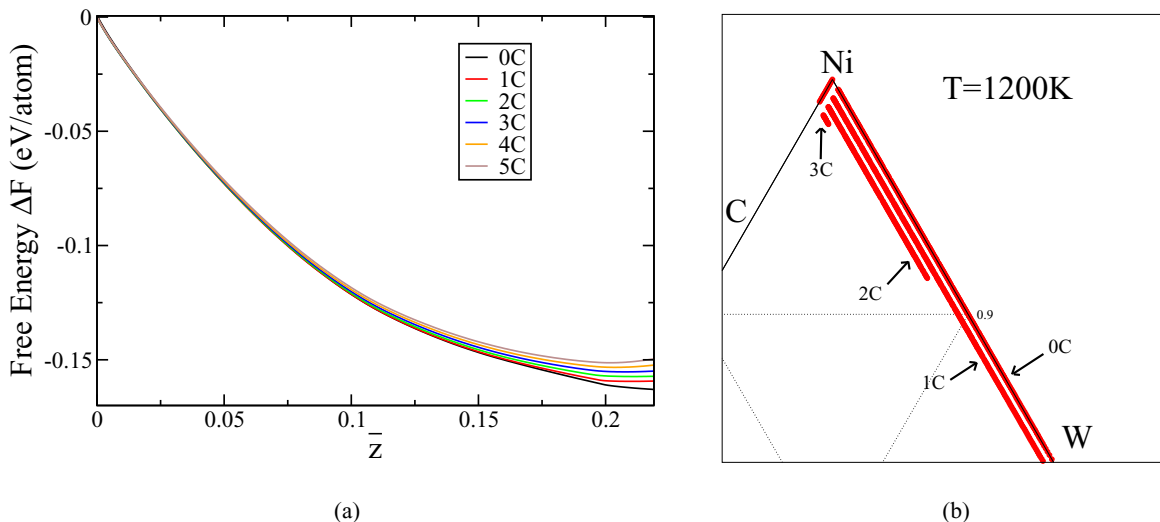
(a)

(b)

FIG. 8. (a) Free energy predicted from simulation from system containing 270 Ni/W atoms, with various numbers of C atoms. (b) Enlargement of the predicted phase diagram at $T = 1200$ K at the high Ni corner. The red dots (connecting as lines) show the stable compositions lying on the convex hull, and occupy the region of stability of a single phase C-Ni-W fcc solid solution. Each line shows the convex hull for each free energy curve with different number of carbon atoms.

we have not performed simulations. We use a piecewise linear function to express the energy because, as shown in Fig. 2, there are two regions with different trends in energies. For the fcc solid solution with interstitial carbon of composition $C_x Ni_y W_z$ ($x + y + z = 1$), the piecewise linear energy can be expressed as

$$E(x, y, z) = x E_C + (y + z) E_{Ni-W}.$$

E_C is determined from C solubility in Ni [30]. E_{Ni-W} is the piecewise linear function of the convex hull of the phases Ni.cF4, Ni$_8$W.tI18, Ni$_4$W.tI10, and W.cI2.

When estimating the entropy, we take a constrained ideal mixing approximation. Write $C_x Ni_y W_z$ as $C_x Ni_y W_z = xC + (y + z) Ni_{\bar{y}} W_{\bar{z}}$, where $\bar{y} = y/(y + z)$, $\bar{z} = z/(y + z)$. Note that the number of octahedral interstitial sites equals the number

of metal sites. Under this constraint (i.e., the assumptions that W atoms have no C as nearest neighbors and that W atoms are widely separated), a fraction $6z$ of interstitial sites must be vacant. These assumptions are reasonable since the C-W bond has an energy of 0.583 eV/bond with respect to the C-Ni bond, and our fitting model yields positive values for the nearest and next nearest W-W pairs. Thus only $(y + z) - 6z = (1 - x) - 6z$ interstitial sites are potentially occupied by C. Defining $\bar{\mathbb{1}} \equiv (1 - x) - 6z \geqslant 0$ as the available carbon site fraction, then we have a constraint $z \leqslant 1/6$. We have entropy

$$-S/k_B = x \ln x + (\bar{\mathbb{1}} - x) \ln (\bar{\mathbb{1}} - x) + F_C(\bar{z})(y \ln \bar{y} + z \ln \bar{z}).$$
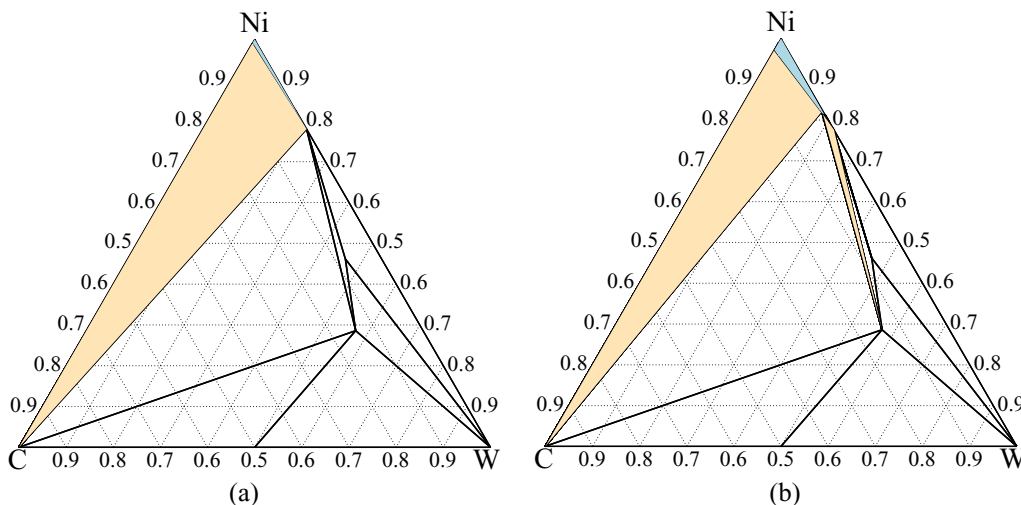
$$(7)$$

(a)

(b)

FIG. 9. C-Ni-W ternary phase diagram derived from Monte Carlo simulations at $T = 1200$ K (a) and $T = 1600$ K (b). The blue shows C-Ni-W fcc solid solution single phase region, the yellow is two-phase region, and the white is three-phase region. Black lines show the convex hull.
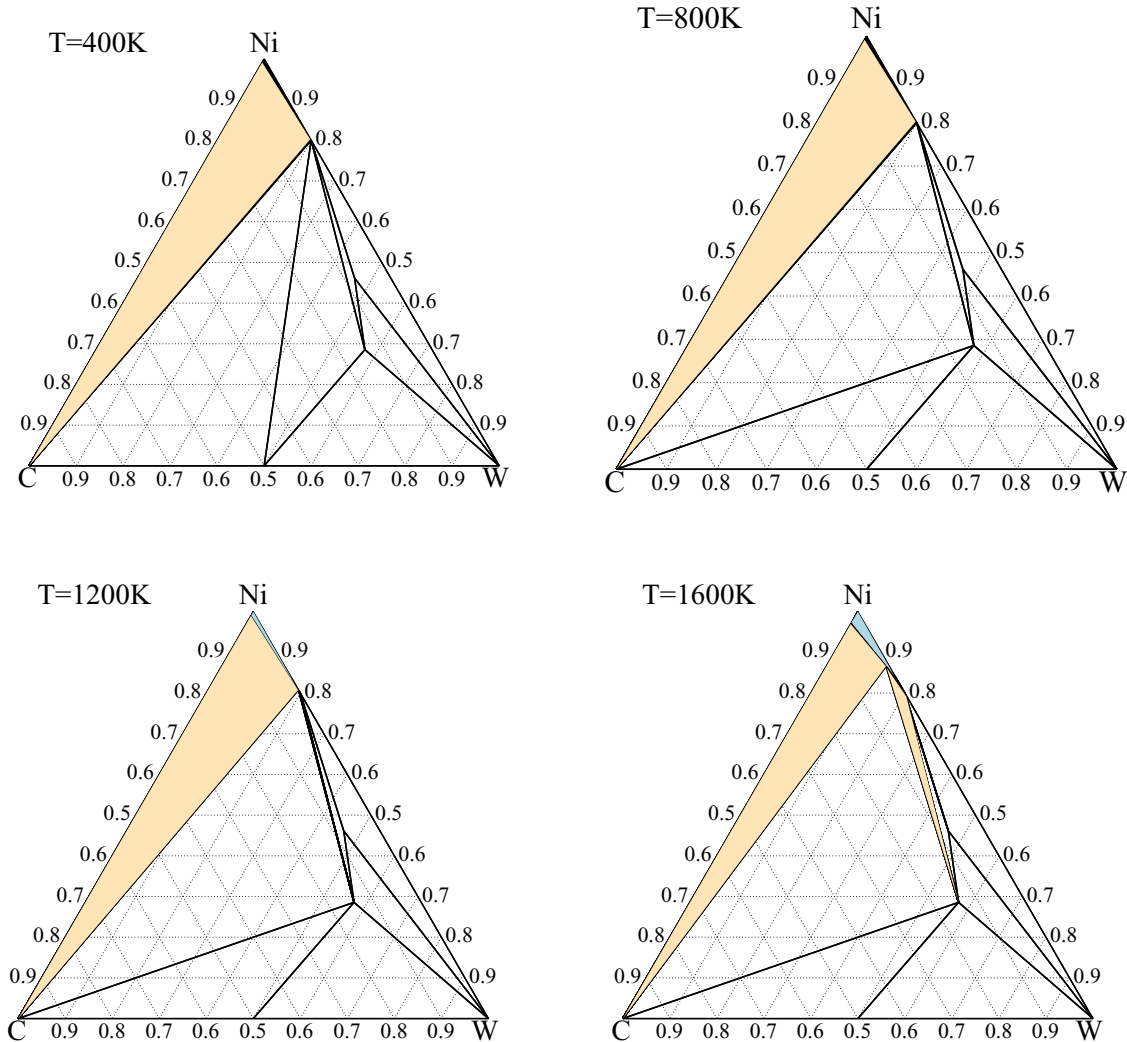
FIG. 10. C-Ni-W phase diagram at $T = 400$ K, 800 K, 1200 K, and 1600 K under the constrained ideal mixing approximation model.

Assuming that the entropy for Ni_4W vanishes (notice the large excitation energy at $x_W = 0.2$ in Fig. 2), we include a factor $F_C(\bar{z}) = 1 - 5\bar{z}$ multiplying the Ni-W entropy since for Ni_4W $\bar{z} = 0.2$, and for pure Ni where $\bar{z} = 0$ we want to keep full entropy.

With this simplified model for the fcc solid solution, together with the free energies of other phases, we predict the phase diagram at various temperatures as shown in Fig. 10. They are similar to the results of our simulations at $T = 1200$ and 1600 K, confirming our heuristic approach. This model also allows us to make predictions at lower temperature, which cannot be reached by simulations due to the difficulty of reaching true thermodynamic equilibrium at lower temperatures. Moreover, this model captures the underlying physics of C impurities limiting the W solubility owing to C-W repulsion, thus providing a possible explanation for the contradiction between the ground state structures predicted at $x_W > 0.2$, while experimentally the Ni-W solid solution terminates at $x_W < 0.16$, which is consistent with our constraint $z \leqslant 1/6$.

IV. CONCLUSION

A superatom model was constructed for fcc solid solutions of Ni-W. This superatom model fits well to density functional theory total energies, serving as an energy model for Monte Carlo simulation. With this model, we first studied the Ni-W binary phase diagram from 0 to 23 at. % tungsten composition. To study the ternary C-Ni-W solid solution, where carbon atoms are at octahedral interstitial sites, we augmented the model by including the carbon-tungsten, and carbon-carbon bond, nearest neighbor repulsion.

Monte Carlo simulations on a grid of temperatures and chemical potentials, together with replica exchange to attain better-equilibrium sampling, reveal a miscibility gap between Ni_8W and Ni_4W at low temperature, but a full solubility range at higher temperatures, above 1000K. At the high μ limit end the tungsten composition is slightly higher than 20 at. %. Including carbon atoms decreases the tungsten composition, especially at the high μ end. Understanding the experimentally reported [7] binary solubility limit of 16% W follows naturally from our constraint $z \leqslant 1/6$ assuming
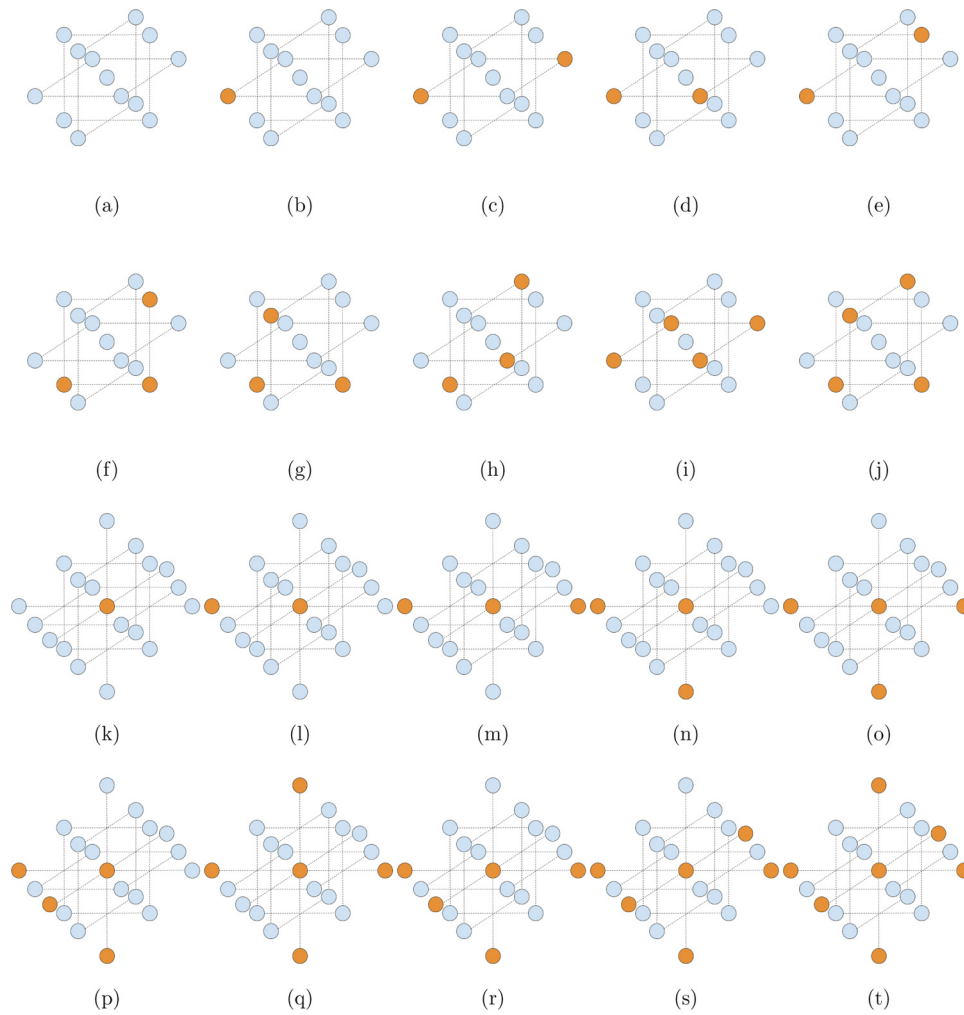
FIG. 11. Twenty types of superatoms. Blue are Ni atoms and orange are W.

the presence of impurities in the (nominally) binary Ni-W samples. The same effect could explain the failure to observe the predicted $Ni_8W.tI18$ structure.

Comparing the free energies predicted from semigrand canonical simulations with those of competing phases calculated by density functional theory, we predicted the phase diagram of the C-Ni-W ternary at multiple temperatures, which also inherently showed the carbon solubility in Ni-W solid solution. A constrained ideal mixing approximation gives similar results, and can serve as a way to predict the phase diagram at lower temperatures. The presence of carbon as impurity leads to a solid solution phase instead of the low temperature stable Ni_8W phase, perhaps explaining why that

phase is not observed in experiment, under the assumption that the experimental samples contain a small percentage of carbon or similar impurities.

APPENDIX

See Fig. 11 for 20 types of superatoms.

[1] R. C. Reed, *The Superalloys: Fundamentals and Applications* (Cambridge University Press, Cambridge, UK, 2008).

[2] N. Eliaz, T. Sridhar, and E. Gileadi, Electrochim. Acta **50**, 2893 (2005).

[3] S. Yao, S. Zhao, H. Guo, and M. Kowaka, Corrosion **52**, 183 (1996).

[4] V. Raghavan, J. Phase Equilib. Diffus. **30**, 281 (2009).

[5] K. Einarsdotter, B. Sadigh, G. Grimvall, and V. Ozoliņš, Phys. Rev. Lett. **79**, 2073 (1997).

[6] A. J. Detor and C. A. Schuh, Acta Mater. **55**, 4221 (2007).

[7] S. N. Naidu, A. Sriramamurthy, and P. R. Rao, J. Alloy Phase Diagrams **2**, 1 (1986).

[8] R. Cury, J.-M. Joubert, S. Tusseau-Nenez, E. Leroy, and A. Allavena-Valette, Intermetallics **17**, 174 (2009).

[9] H. Okamoto, J. Phase Equilib. **12**, 703 (1991).

[10] N. Schindzielorz, K. Nowak, S. Maisel, and S. Müller, Acta Mater. **75**, 307 (2014).

[11] S. B. Maisel, N. Schindzielorz, S. Mueller, H. Reichert, and A. Bosak, J. Appl. Crystallogr. **46**, 1211 (2013).

[12] C. J. Marvel, P. R. Cantwell, and M. P. Harmer, Scr. Mater. **96**, 45 (2015).

[13] G. Kresse and J. Hafner, Phys. Rev. B **47**, 558 (1993).

[14] G. Kresse and J. Hafner, Phys. Rev. B **49**, 14251 (1994).

[15] G. Kresse and J. Furthmüller, Comput. Mater. Sci. **6**, 15 (1996).

[16] G. Kresse and J. Furthmüller, Phys. Rev. B **54**, 11169 (1996).

[17] P. E. Blöchl, Phys. Rev. B **50**, 17953 (1994).

[18] G. Kresse and D. Joubert, Phys. Rev. B **59**, 1758 (1999).

[19] J. P. Perdew, K. Burke, and M. Ernzerhof, Phys. Rev. Lett. **77**, 3865 (1996).

[20] J. P. Perdew, J. Chevary, S. Vosko, K. A. Jackson, M. R. Pederson, D. Singh, and C. Fiolhais, Phys. Rev. B **48**, 4978 (1993).

[21] A. Ektarawong, S. I. Simak, L. Hultman, J. Birch, and B. Alling, Phys. Rev. B **90**, 024204 (2014).

[22] M. H. F. Sluiter and Y. Kawazoe, Phys. Rev. B **68**, 085410 (2003).

[23] A. M. Ferrenberg and R. H. Swendsen, Phys. Rev. Lett. **61**, 2635 (1988).

[24] A. M. Ferrenberg and R. H. Swendsen, Phys. Rev. Lett. **63**, 1195 (1989).

[25] S. Yao, W. P. Huhn, and M. Widom, Solid State Sci. **47**, 21 (2015).

[26] C. J. Marvel, Ph.D. thesis, Lehigh University, 2016.

[27] F. C. Frank and J. S. Kasper, Acta Crystallogr. **11**, 184 (1958).

[28] M. Fiedler and H. Stadelmaier, Z. Metallkd. **66**, 402 (1975).

[29] H. Okamoto, J. Phase Equilib. Diffus. **29**, 543 (2008).

[30] T. B. Massalski, H. Okamoto, P. Subramanian, and L. Kacprzak, ASM Intl. **1990**, 1485 (1990).